High–Resolution Imaging and Spectroscopy of Multipolar Plasmonic Resonances in Aluminum Nanoantennas

6 AUTHORS, INCLUDING:

Mathieu Kociak
French National Centre for Scientific Research
143 PUBLICATIONS **3,877** CITATIONS

Julien Proust
Institut Fresnel
16 PUBLICATIONS **73** CITATIONS

Davy Gérard
Université de Technologie de Troyes
72 PUBLICATIONS **861** CITATIONS

Jérôme Plain
Université de Technologie de Troyes
123 PUBLICATIONS **1,168** CITATIONS

# High-Resolution Imaging and Spectroscopy of Multipolar Plasmonic Resonances in Aluminum Nanoantennas

Jérôme Martin,*,[†] Mathieu Kociak,*,[‡] Zackaria Mahfoud,[†,‡] Julien Proust,[†] Davy Gérard,[†] and Jérôme Plain[†]

[†]Institut Charles Delaunay — Laboratoire de nanotechnologies et d'instrumentation optique, UMR CNRS 6281, Université de Technologie de Troyes, Troyes 10010, France

[‡]Laboratoire de Physique des Solides, Bâtiment 510, UMR CNRS 8502, Université Paris Sud, Orsay 91400, France

ABSTRACT: We report on the high resolution imaging of multipolar plasmonic resonances in aluminum nanoantennas using electron energy loss spectroscopy (EELS). Plasmonic resonances ranging from near-infrared to ultraviolet (UV) are measured. The spatial distributions of the multipolar resonant modes are mapped and their energy dispersion is retrieved. The losses in the aluminum antennas are studied through the full width at half-maximum of the resonances, unveiling the weight of both interband and radiative damping mechanisms of the different multipolar resonances. In the blue-UV spectral range, high order resonant modes present a quality factor up to 8, two times higher than low order resonant modes at the same energy. This study demonstrates that near-infrared to ultraviolet tunable multipolar plasmonic resonances in aluminum nanoantennas with relatively high quality factors can be engineered. Aluminum nanoantennas are thus an appealing alternative to gold or silver ones in the visible and can be efficiently used for UV plasmonics.

KEYWORDS: Electron Energy Loss Spectroscopy, Plasmonics, Aluminum, Multipoles, Losses, Q Factor
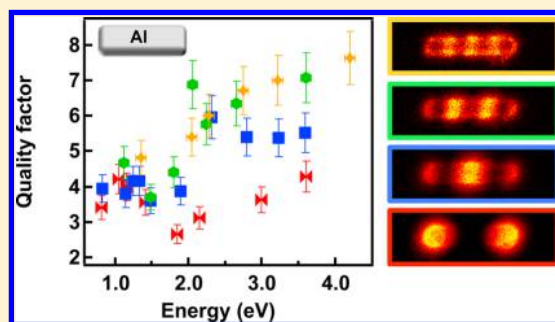
Plasmonics has a tremendous potential for a wide range of applications including enhanced light-matter interaction,[1] energy harvesting,[2] and highly sensitive detection of chemicals.[3] Nowadays, plasmonics relies mostly on nanostructures made of noble metals, essentially gold and silver. However, these metals have inherent limitations hindering the development of plasmonic devices toward the blue and ultraviolet (UV) parts of the spectrum. Gold does not exhibit plasmonic resonances at wavelengths shorter than 520 nm due to its interband transitions. Silver nanostructures exhibit resonances down to 350 nm but suffer from strong oxidation and lose their plasmonics properties over time. Overcoming those issues, aluminum plasmonics is now emerging. A rapidly increasing number of paper underlines its potential and demonstrates that aluminum nanostructures exhibit surface plasmon resonances down to the deep UV (below 200 nm), with moderate losses.[4−9] In striking contrast with noble metals, aluminum is an inexpensive and abundant material, a key advantage for commercial and industry-related applications. Moreover, aluminum is compatible with optoelectronic devices and CMOS technology. For instance, aluminum opens avenues for plasmonic engineering of the optical properties of wide bandgap semiconductors such as ZnO[10] or GaN related alloys.[11] Last, aluminum plasmonics is also very promising for metal enhanced fluorescence,[12,13] enhanced Raman spectroscopy,[14,15] or label-free biosensing applications.[16]

Of paramount importance in the development of future aluminum plasmonic devices is the capability to characterize aluminum nanostructures at the nanometer scale. Most studies report only ensemble measurements (extinction spectroscopy). In ref 5, Knight and co-workers have imaged radiative Al nanoantenna resonances (dipolar and quadrupolar plasmonic modes) using energy-filtered cathodoluminescence with a spatial resolution of 20 nm. The experimental part of the study was, however, restricted in spectral range and resolution and to radiative modes only. In particular, they could not investigate experimentally the dissipation related to individual nanoantennas. Resolving the different plasmonic modes spatially and spectrally sustained by a single Al nanoantenna with nanometer resolution has still to be demonstrated. In this Letter, we show that electron energy loss spectroscopy (EELS), a powerful tool based on the excitation and detection of surface plasmons by an electron beam,[17−21] is able to unveil spatially and spectrally multipolar plasmonic modes sustained by a single aluminum nanoantenna. We obtain high-resolution EELS hyperspectral images of individual Al nanoantennas, thereby revealing the spatial and spectral distribution of the multipolar plasmonic modes. The resonances span a wide spectral region, from near-infrared to ultraviolet. By studying their line widths, we unveil the weight of both interband and radiative damping mechanisms of the plasmonic modes. At a given energy in the blue-UV region, high order modes sustained by high aspect

ratio nanoantennas have reduced losses compared to dipoles sustained by low aspect ratio nanoantennas. This phenomenon is attributed to the reduction of both radiative and interband damping for high order modes. Consequently, the quality factors of multipolar resonances are about two times higher than the quality factors of dipoles in the blue-UV region. This study demonstrates that aluminum nanoantennas are very appealing to achieve controlled plasmonic properties in the near-infrared to ultraviolet, offering a viable alternative to noble metals, and are particularly promising for efficient UV plasmonics.

Aluminum nanoantennas consisting of nanorods were fabricated by electron beam lithography and lift-off process[22] on a STEM-EELS compatible substrate, that is, a 30 nm thick Si_3N_4 membrane. The length of the nanorods varies from 60 nm to 1 μm while keeping a 60 nm constant width. The thickness of all structures is set to 40 nm. The aspect ratio is arbitrarily defined as the length divided by the width. EELS measurements were carried out using a NION USTEM 200 scanning transmission electron microscope (STEM) fitted with a cold field emission gun. The EELS spectrometer is fitted with a high sensitivity CCD camera. EELS data were acquired in the spectral image mode (SI), where a spectrum is acquired at each pixel of a scan, together with the high-angle annular dark field (HAADF) signal. At the end of the scan, both an SI and an HAADF image are generated, which can be compared pixel per pixel. In this study, we worked at 100 keV, with a typical 20 pA, 30 mrd half angle (less than 1 angström) electron beam. Typical dwell times per pixel were 8−10 ms, and SIs were typically 200 × 100 pixels. We kept almost the same aspect ratios and number of pixels for each SI, and adapted the spatial sampling to the varying sizes of the structures. Starting with a spectral resolution of 0.4 eV, systematic Richardson−Lucy deconvolution[23] (with typically 50 iterations) allowed us to get a typical 0.15 eV resolution. This allowed us to study the low energy part of the spectrum, which could not be unveiled in the pioneering work of Batson[24] on aluminum spheres. Further automatic fitting using several Gaussians were used to generate energy position, intensity, and full width at half maximum (FWHM) maps[21] through an IGOR pro homemade set of routines.[25]

Figure 1 presents typical deconvoluted EEL spectra measured on an aluminum nanorod, with the HAADF image of the corresponding nanoantenna shown in the inset. The spectra are taken from the three squared areas drawn on the HAADF image inset and are, therefore, a sum of individual spectra contained in the area. The EEL spectra reveal well-resolved distinct energy loss peaks centered at 1.4, 2.8, 3.6, 4.3, and 4.7 eV depending on where they are measured from the antenna. These peaks correspond to even and odd multipolar plasmonic resonances supported by the Al antenna (dipole $m = 1$; quadrupole $m = 2$ and following modes of order up to 5), as it will be evidenced in the following. For every nanorod, a broad peak appears around 6−8 eV, which corresponds to the electrostatic plasmon (i.e., the surface plasmon at the interface between Al and a dielectric medium) as shown later thanks to numerical calculations. A very high loss peak centered at 15 eV corresponding to the aluminum bulk plasmon was measured for every structure but is not visible on the figure due to the chosen scale. On most spectra, close inspection revealed a peak around 1.5 eV ± 0.2 eV, sometimes convoluted with another plasmonic resonance. This feature is attributed to the interband transitions of aluminum and will be discussed later. Measurements were
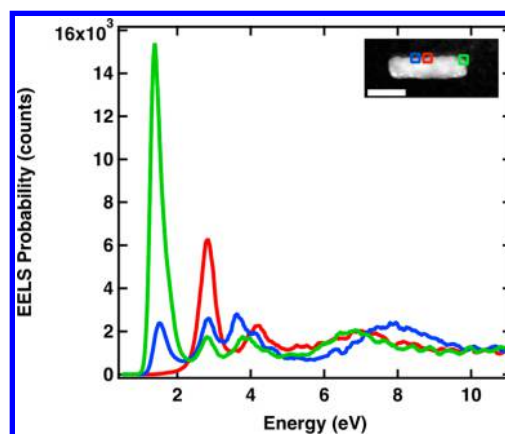

Figure 1. EEL spectra acquired at different locations on a single Al nanorod as indicated through a color code in the inset. The spectra have been deconvoluted 30 times and summed over 10 × 10 pixels. Inset: corresponding HAADF−STEM image. Scale bar 100 nm.

also performed on larger antennas and showed energy loss peaks centered at energies down to 0.8 eV, corresponding to plasmon modes in the near-infrared. On the other hand, smaller structures showed multipolar plasmon modes up to 4.7 eV. The broadband nature of the optical properties of the aluminum antennas is evidenced as they sustain multipolar plasmonic resonances spanning the electromagnetic spectrum from the near IR to the mid UV, as confirmed in the following.

The nature of the modes is best ascertained by mapping their physical properties. In Figure 2, we map the intensity (left panel), FWHM (central panel), and energy position (right panel) for the first four modes of a representative nanorod. The very well-defined energy and FWHM maps makes us confident that, within our spectral resolution, individual modes spatially coherent over the whole nanorod have been identified.[21] This has been reproduced on all nanoantennas investigated in this study, even if modes with energies lower than 0.8 eV where difficult to measure due to our set up limitations, as well as high-energy modes due to reduced signal-to-noise ratio and visibility between two modes. The intensity maps, related to the electromagnetic local density of states (EMLDOS)[19,21] projected along the electron beam direction, reveal oscillations typical for standing waves as probed by EELS,[17,26,27] especially in the case of nanorods.[28−30] The modes are thus multipolar modes of the nanoantennas. Interestingly, due to the high density of free electrons in aluminum (three times higher than that of noble metals) and the subsequent high value of its bulk plasma frequency, the resonances are well separated in the energy space, especially when compared to resonances supported by silver or gold antenna.[31] As we will see in the following, the dispersion relation of the Al nanoantennas does not differ significantly from those of silver and gold except, of course, for its broader range in the UV. In addition to this expected broader range, the main difference between the plasmonic properties of aluminum and those of gold or silver concerns the FWHM and quality Q factors, as it will be discussed thoroughly later.

In order to interpret our experimental results, we performed different simulations on Al cylindrical nanorods of 60 nm diameter and various lengths embedded in media of various indexes using the MNPBEM package[32] and its EELS extension.[33] Although it is a simplified model compared to the experimental nanoantennas, it will prove to be in good
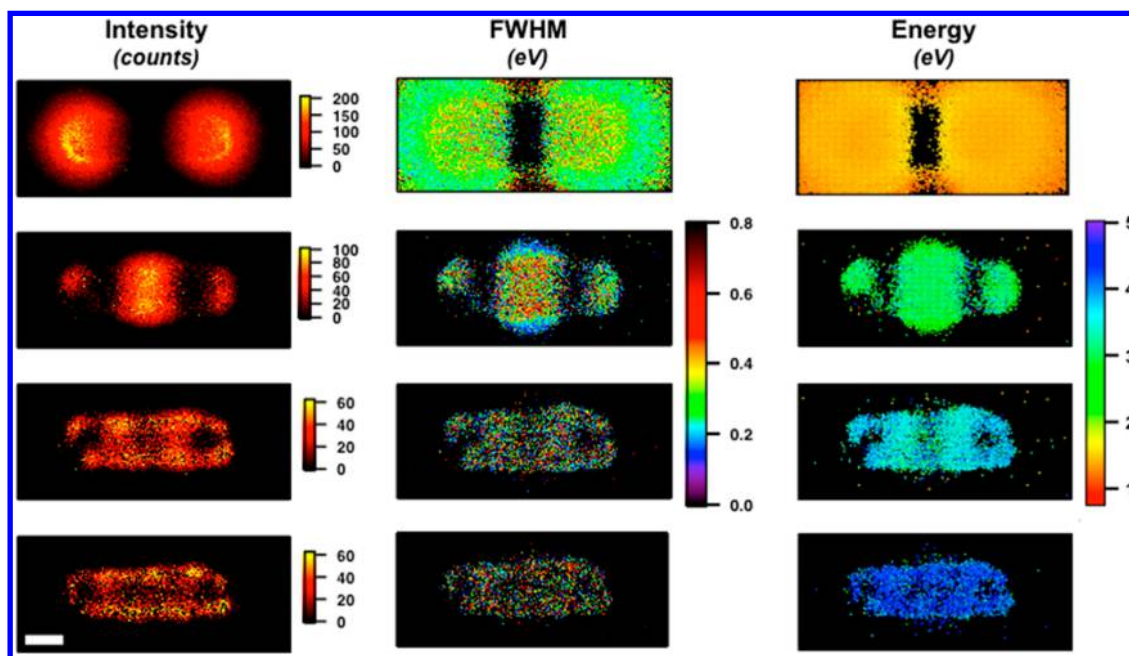
Figure 2. Experimental EELS intensity, FWHM, and energy position maps of the main plasmonic resonances sustained by a typical Al nanorod. The intensity maps are centered at 1.4, 2.8, 3.6, and 4.3 eV (from top to bottom) corresponding to the $m = 1$ to $m = 4$ modes (see text). Scale bar is 50 nm in bottom left map (same for all maps).

agreement with the experimental results while giving useful hints on the physics of dissipation in aluminum nanoantennas. We used a Drude−Lorentz model for the Al dielectric constant, which has shown to be in excellent agreement with experimental optical results.[34] We have performed EELS and cathodoluminescence (CL) spectra simulations for various lengths of the nanorods, when the beam is five nanometers away from the end of the nanorod, along its axis. The EELS spectra were calculated using the regular MNPBEM functions[33] based on the theory of Garcia de Abajo and Howie.[35] The CL spectra have been computed as the power emitted along a 4π steradians solid angle at infinity, divided by $k = \omega/c$, where ω is the energy and c the speed of light in the medium.[20] We show in Figure 3 the results for two different sizes of nanorods surrounded by a dielectric medium with a refractive index of 1.5. The EELS and CL spectra have been normalized to the intensity of their dipolar modes. The expected series of multipolar peaks, as well as the electrostatic plasmon clearly appear. We note that the electrostatic plasmon arises around 7 eV, as in the case of our experiment. The antenna, thus, is behaving as if it was surrounded by an effective medium with $n = 1.5$, an assumption often made to describe plasmonic objects on a substrate.[36] With respect to EELS, the CL intensity drops rapidly for higher multipolar modes. For a given mode, the ratio between the CL and EELS peak intensities is a good indication of its radiative properties. Indeed, this ratio allows determining the relative weights of radiative and nonradiative damping mechanisms of a given plasmonic mode. For instance, around 4.2 eV the shorter nanorod sustains a highly radiative quadrupolar resonance (similar EELS and CL peak intensities), whereas for the longer nanorod, the resonance of order $m = 8$ located at the same energy is weakly radiative. Finally, we point out that the plasmonic resonances sustained by the high aspect ratio nanorod are significantly narrower than the ones sustained by the low aspect ratio nanorod. An experimental confirmation of these elements is given below.

In the following, we study the dispersion relations of the multipolar resonances, and their losses through their line widths. The establishment of multipolar plasmonic resonant modes in finite metallic nanostructures can be understood as standing surface plasmon polariton (SPP) waves resulting from Fabry−Pérot resonances in the considered structure.[28,29,37,38] By plotting the position of the energy loss peak of each mode with respect to its associated SPP wavevector (noted k_{sp}), we can retrieve the dispersion relations of the multipolar plasmonic resonances. The wavevectors are measured by extracting line profiles from EELS amplitude maps as $k_{sp} = 2\pi/\lambda_{sp}$. Here, the value of the half-wavelength $\lambda_{sp}/2$ is directly measured from EELS intensity maps and is equal to the distance between adjacent antinodes. One example of wavevector extraction is given in Figure 4a for an even plasmonic resonant mode ($m = 4$) with a corresponding energy of 2.0 eV supported by a 650 nm long aluminum nanorod. Interestingly, and in contrast with the well-known theoretical case of a one-dimensional standing wave, the spacing between adjacent maxima decreases as the supported standing wave gets close to the ends of the nanorod. The variation of λ_{sp} throughout the length of a nanorod has already been observed in Ag nanowires and nanorods in previous studies[28,29] and is known as "λ_{sp}-compression" or "antinode bunching". The lowest value of k_{sp} (or higher value of λ_{sp}) is close to the center of the Al antenna, whereas k_{sp} is getting higher values when approaching the ends of the nanorod. Up till now, the origins of this phenomenon are not fully understood.

From Figure 4b, it appears that the multipolar plasmonic resonances follow a dispersion relation close to the fundamental surface plasmon polariton mode sustained by an infinitely Al long nanorod (or slab) over a dielectric substrate. The dispersion curve was also retrieved using BEM simulations, for two effective refractive indexes, $n = 1.5$ and $n = 2$ (circles in Figure 4b). The experimental results at low energy are best fitted by simulations performed for an effective refractive index
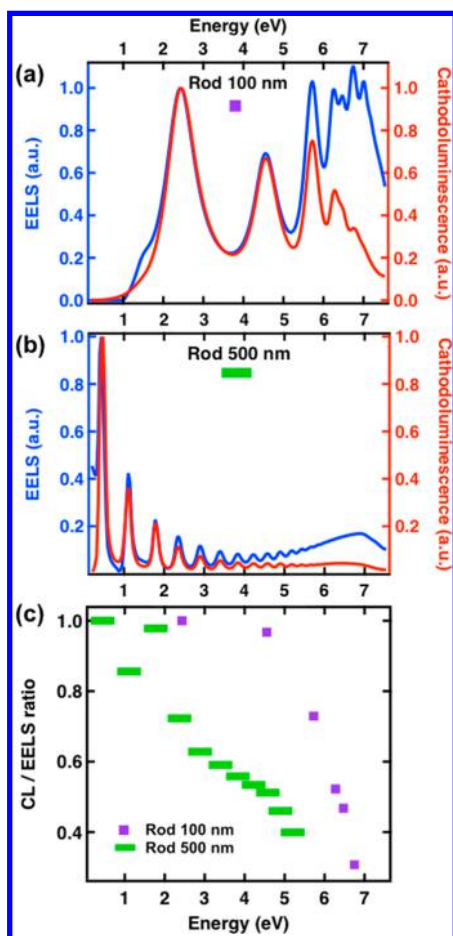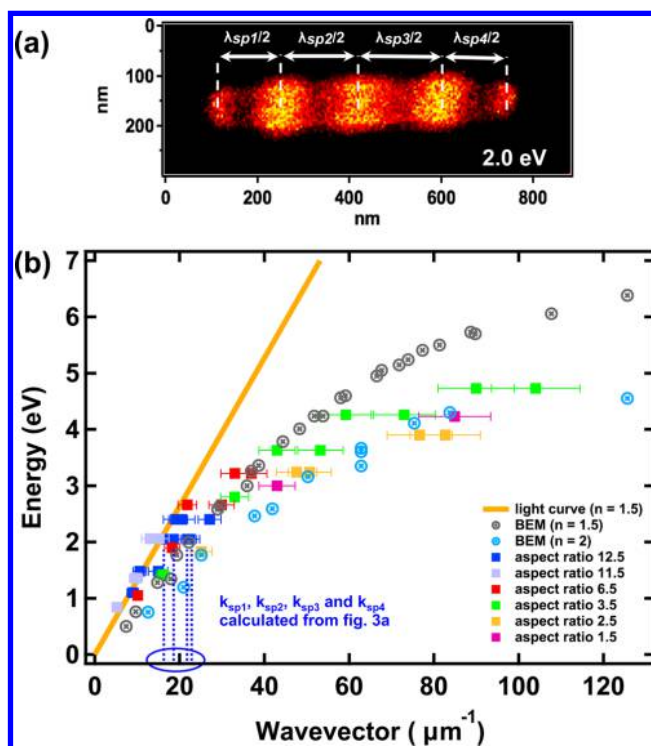
Figure 3. BEM simulations of the EELS and CL spectra for an electron beam of 100 keV, 5 nm away from the end of Al nanorods embedded in a medium of refractive index 1.5 with length (a) 100 nm and (b) 500 nm. The diameter of the rod is 60 nm in both cases. The EELS and CL spectra are normalized to the maximum of their respective dipolar peaks. (c) Ratio of the CL to EELS intensity, normalized to the dipolar intensity value for each mode as a function of the energy for the two rods.

Figure 4. (a) Example of λ_{sp} extraction from a line profile taken on an EELS map. The four annotated values of λ_{sp} correspond to the four measured distances between antinodes (b) Multipolar plasmonic resonances dispersion relations for several Al nanoantennas. The numbers in the legend refer to the nanorods aspect ratio. For each antenna, the first point is associated with the dipolar mode, except for the longer antenna (12.5 aspect ratio), for which the first point corresponds to the quadrupolar mode. Circles are EELS peak positions deduced from BEM calculations for several Al antennas geometries with an effective refractive index of 1.5 and 2.

$n = 1.5$; that is, the average index between the substrate and the vacuum. However, discrepancies appear at high energy, where the experimental points are closer to the $n = 2$ calculated dispersion curve. This shows that the effective refractive index increases with the wavevector. This phenomenon can be explained by considering that high-order modes are more confined inside the native oxide shell.

As observed above, the modes are spanning a wide range of energy, from the near-infrared (typically 0.8 eV) to the mid-UV (up to 4.7 eV). We note that the dispersion curve is close to the light line in an effective medium of index $n = 1.5$ (blue line in Figure 3b) for wavevectors up to 20 μm^{-1} corresponding roughly to an energy of 2 eV. This detail is of importance as it reveals that multipolar plasmonic resonances sustained by Al nanoantennas can be easily coupled to light from the near IR to visible, at least below 2 eV. This behavior differs from what is observed for Au and Ag resonant modes as their dispersion curve start to bend earlier at lower values of k_{sp} vectors.[31] This is because the energy of any surface plasmon in nanoantennas converges to that of an infinite half plane (i.e., to the electrostatic plasmon energy value) and can never be higher than the bulk plasmon energy.[21] Both energies are higher in Al

than in Ag and Au. In the present experiment, the retarded regime of Al multipolar plasmonic modes, therefore, is unveiled for energies up to 2 eV but could probably be increased using a substrate with lower index and, thus, higher electrostatic surface plasmon energy.

We now turn to the dissipation mechanisms and strength of the plasmonic modes in Al. Generally speaking, two main damping mechanisms can be distinguished: interband (IT) and radiative damping (as the intraband damping can be considered constant at a given temperature). In the case of aluminum, IT transitions are localized in a relatively narrow range of energy centered at 1.5 eV. Al plasmons dissipation, therefore, is expected to be extremely important within this energy band. As a result, the line width or FWHM of Al plasmons increases if they are tuned to resonate inside this band. Zoric and co-workers[39] showed that the line widths of dipolar resonances supported by Al nanodisks rapidly increase as a function of their energy, with a first maximum located at 1.8 eV close to the IT transition. This maximum arises on a continuously increasing "background" of radiative damping reaching its highest values in the near-UV range. As a result, the line widths remain high even above the IT region, keeping values greater than or equal to 0.8 eV in the blue/UV range. Such relatively broad dipolar resonances may appear detrimental for some applications. Thus, it is worth examining the situation in the more favorable case of nanorods, where the IT and radiative damping effects may be optimized.[40] Also, as the multipolar
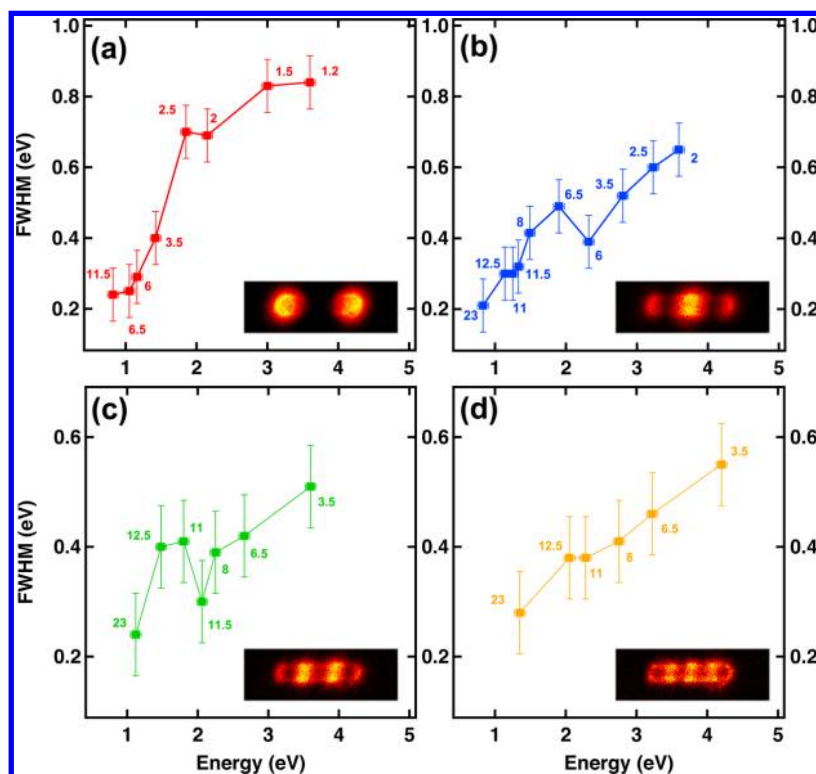
Figure 5. Measured values of the line widths of multipolar peaks as a function of their resonance energy for (a) $m = 1$ modes, (b) $m = 2$ modes, (c) $m = 3$ modes, and (d) $m = 4$ modes. The numbers close to each point correspond to the aspect ratio of the corresponding nanoantenna. Note that the 11.5 aspect ratio antenna has slightly higher values of energy compared to the 11 aspect ratio antenna for a given mode, a deviation remaining within the error bars.

modes most probably couple less to light (see, e.g., the departure from the light line of the multipolar modes above 2 eV in Figure 3), it is also worth examining separately the situation for multipolar modes.

In Figure 5, the line widths of the multipolar plasmonic resonances (of orders ranging from $m = 1$ to $m = 4$) are plotted with respect to their corresponding energy maxima. In order to get a reliable value for the FWHM, they have been measured on spectra summed around pixels of the SI where the intensity of the given mode is maximum. As the energy of a particular mode is dependent on the antenna geometry, the antenna aspect ratio is annotated next to each experimental point. A general observation is that the FWHM, although probably slightly overestimated due the finite spectral resolution of the setup, are relatively high compared to what is found in silver or gold, as already noted by Zoric et al.[39] in the case of Al nanodisks. However, a clear difference is seen between the dipolar and multipolar modes. Although the FWHM of the former is rapidly increasing for energy below 2 eV, and then increasing at a lower rate, multipolar modes exhibit a relatively clearer local maximum at the IT energy superimposed on an almost linear increase.

The trend for the dipolar modes (Figure 5a) is very similar to what was observed by Langhammer et al.[4] The rapid increase of the FWHM finishing slightly above the IT energy is attributed to IT damping plus the underlying increasing radiative damping mentioned above. The local maximum at the IT energy is not clearly visible due to uncertainties. Above IT transitions, the dipolar modes line widths are still high in the blue-UV region because of this underlying slow but continuous increase of radiative losses. Reaching the UV region, the losses of the

dipolar modes are mostly driven by radiative damping.[39] Although nanorods are considered here, damping mechanisms similar to those of nanodisks drive the lifetime of the dipolar modes. This remark is particularly true at high energies (>3 eV) as Al nanoantennas sustaining dipolar resonances in the near UV have an aspect ratio close to unity and, therefore, a geometry relatively close to disk.

We now focus on the higher order modes. Quadrupolar resonances (Figure 5b) exhibit a similar trend to those of dipolar ones, with lower FWHMs in the blue-UV range. The IT energy also appears as a local maximum. We attribute this effect to the reduction of the radiative damping (with respect to the dipolar modes), which makes the nonradiative damping mechanism predominant in higher order resonances. This is confirmed by the simulations that show a reduced CL emission intensity with respect to the EELS intensity for higher order modes for a given nanoantenna (Figure 3). For $m = 3$ and $m = 4$ resonances (respectively, Figure 5c and d), the damping reduction is even stronger, leading to FWHMs typically below 0.6 eV in the blue-UV range. The IT local maximum is harder to see on the FWHMs curves within the experimental errors. Altogether, Figure 5 suggests the following rule of thumb: *the higher the aspect ratio of the antenna, the narrower the line width of the corresponding supported plasmonic resonances.* The BEM simulations (Figure 3) already showed this behavior. Looking back to Figure 4b, it appears that all resonant modes occurring within this spectral range move away from the line curve unveiling their increasingly quasi-static behavior above 2 eV and the subsequent reduction of radiative damping. This effect is combined with the reduction of IT damping outside the 1.5 eV region, leading to the line width reduction of multipolar

plasmonic resonances with respect to dipolar ones in the blue-UV region. The BEM simulations again ascertain this behavior. For a given energy range, the ratio between the CL and EELS intensities decreases for higher order modes (higher aspect ratio), a clear indication that the radiative damping, at a given energy, decreases with the order of the mode (and thus the aspect ratio of the nanoantenna).

The Q factor is an important value to characterize plasmonic resonances as it directly determines the local field enhancement in the vicinity of the nanoantenna. The quality factors (energy divided by line width) calculated from Figure 5 are displayed in Figure 6. It clearly appears that dipolar modes have relatively
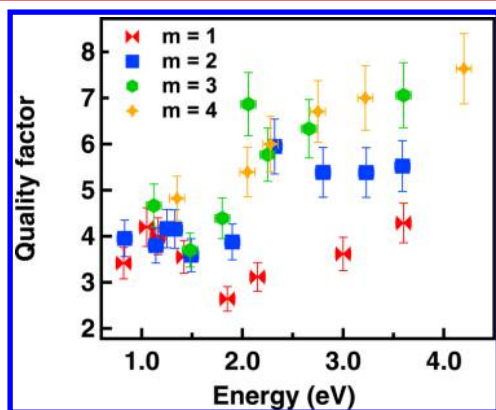
Figure 6. Measured quality factors of several multipolar peaks as a function of their energy of resonances.

low Q factors, typically between 2 to 4 within the whole near IR to UV region. The lower value ($Q \sim 2$) is located at 1.8 eV, close to the IT transition. These values are lower than those from dipolar modes supported by Au ($Q = 10$ to 20)[40] and Ag ($Q = 5$ to 10)[41] nanorods in the near IR to green region. This is a consequence of both IT and radiative damping mechanisms decreasing the dipolar lifetime as detailed earlier and making Al a poorer dipolar plasmonic resonator in the IR-VIS range compared to noble metals. Two regions can be distinguished from Figure 6. Below the interband transition (0.8 to 1.5 eV), all the multipolar resonances present roughly the same Q factor. Above IT, the Q factor of quadrupolar resonances is almost twice their dipolar counterparts. Q reaches even higher values for $m = 3$ and $m = 4$ modes, typically $4 < Q < 8$. The

enhancement of the Q factor for multipoles in comparison to dipoles stems from the diminution of both radiative and interband dampings mentioned above. We conclude that the better way to achieve relatively high-Q UV plasmonic resonances is the use of multipoles sustained by high aspect ratio Al nanoantennas.

In this study, EELS revealed a systematic peak centered around 1.5 eV. The line widths of the resonant plasmonic modes located close to this peak increase due to the associated nonradiative damping. We exemplify its spectral and spatial behavior in Figure 7. Figure 7a shows the spectrum measured on the extremity of a small aspect ratio structure. It clearly shows the presence of a peak around 1.5 eV. This is expected for the IT of Al. Whenever possible, this contribution has been taken into account during the fitting procedure of the SI. On Figure 7b, the result of the fit for this feature and the dipolar mode are presented.

Although the spatial distribution of the dipolar mode has marked maxima at both extremities of the rod, the other feature has a much more uniform spatial distribution. This feature has been encountered on all nanoantennas. This is expected for the spatial distribution of the IT, which is not a spatially coherent excitation.[42,43] Because it arises around 1.5 eV whatever the aspect ratio of the nanoantenna and does not exhibit marked spatial distribution, this feature is safely attributed to the main Al IT. A slight increase of the IT signal at the tips of the nanoantenna can however be seen, which is now under systematic investigation. We note that the IT signal can be detected even outside of the nanoantenna, a counterintuitive but well-understood behavior of IT as probed in EELS (see, for example, refs 42 and 43).

In summary, we used STEM-EELS to characterize the multipolar plasmonic resonances supported by individual aluminum nanoantennas. Depending on their order and the geometry of the nanoantenna, the resonant modes span energies ranging from the near IR to the UV part of the electromagnetic spectrum. Considering multipoles as the result of Fabry−Pérot standing waves, we measured the SPP wavevectors from EELS maps for each mode and retrieved their energy dispersion relations. By measuring the FWHM of the multipolar plasmonic resonances, we have studied their damping mechanisms. In the blue-UV spectral range, high order modes have reduced FWHM compared to low order modes resonating at the same energy due to both a reduction of radiative and IT damping. Nonradiative contribution is also
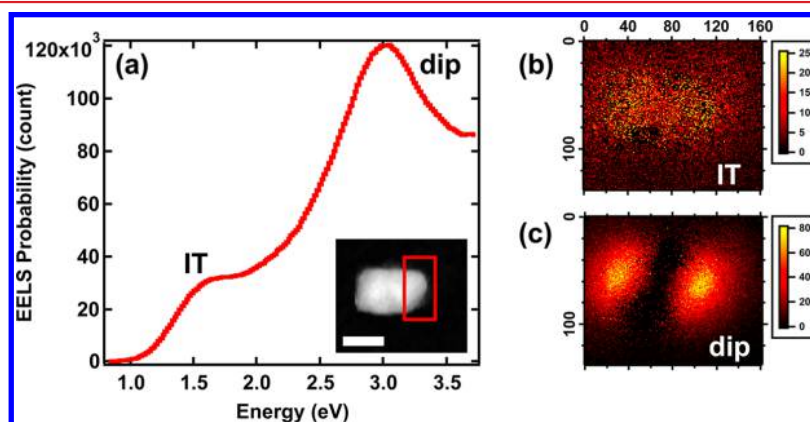
Figure 7. (a) EEL spectra averaged over the red square in the HAADF-STEM image in inset for a 1.5 aspect ratio Al nanorod. Scale bar 50 nm. (b) Gaussian-fitted EELS amplitude maps unveiling the spatial distributions of the IT (b) and the dipolar mode (c).

unveiled for the resonant modes occurring within the energy window where Al bulk interband transitions are active. Finally, the quality factors of the multipolar resonances are calculated. The Q factors are dependent on the order of the mode. For a given value of energy within the blue-UV region, high order multipolar plasmonic resonances sustained by Al antennas with high aspect ratio present a 2-fold higher Q factor than dipolar resonances sustained by antennas with low aspect ratio. This study demonstrates that EELS is a very powerful tool to characterize thoroughly the multipolar plasmonic resonances sustained by aluminum nanostructures. Aluminum-based plasmonics is hence not limited to UV applications but is tremendously appealing for the next generation of plasmon-based nanooptics tunable from the near IR to the UV wavelengths.

■ AUTHOR INFORMATION

Corresponding Authors
*E-mail: mathieu.kociak@u-psud.fr.
*E-mail: jerome.martin@utt.fr.
Notes
The authors declare no competing financial interest.

■ ACKNOWLEDGMENTS

■ REFERENCES

(1) Tam, F.; Goodrich, G.; Johnson, B.; Halas, N. J. *Nano Lett.* **2007**, 496−501.

(2) Atwater, H. A.; Polman, A. *Nat. Mater.* **2010**, *9*, 205−213.

(3) Willets, K. A.; Van Duyne, R. P. *Annu. Rev. Phys. Chem.* **2006**, *58*, 267−297.

(4) Langhammer, C.; Schwind, M.; Kasemo, B.; Zoric, I. *Nano Lett.* **2008**, *8*, 1461−1471.

(5) Knight, M. W.; Liu, L.; Wang, Y.; Brown, L.; Mukherjee, S.; King, N. S.; Everitt, H. O.; Nordlander, P.; Halas, N. J. *Nano Lett.* **2012**, *12*, 6000−6004.

(6) Taguchi, A.; Saito, Y.; Watanabe, K.; Yijian, S.; Kawata, S. *Appl. Phys. Lett.* **2012**, *101*, 081110−081110−4.

(7) Maidecchi, G.; Gonella, G.; Proietti Zaccaria, R.; Moroni, R.; Anghinolfi, L.; Giglia, A.; Nannarone, S.; Mattera, L.; Dai, H.-L.; Canepa, M.; Bisio, F. *ACS Nano* **2013**, *7*, 5834−5841.

(8) Martin, J.; Proust, J.; Gerard, D.; Plain, J. *Opt. Mater. Express* **2013**, *3*, 954.

(9) Knight, M. W.; King, N. S.; Liu, L.; Everitt, H. O.; Nordlander, P.; Halas, N. J. *ACS Nano* **2014**, *8*, 834−840.

(10) Lawrie, B. J.; Kim, K.-W.; Norton, D. P.; Haglund, R. F. *Nano Lett.* **2012**, *12*, 6152−6157.

(11) Okamoto, K.; Niki, I.; Shvartser, A.; Narukawa, Y.; Mukai, T.; Scherer, A. *Nat. Mater.* **2004**, *3*, 601−605.

(12) Malicka, J.; Gryczynski, I.; Gryczynski, Z.; Lakowicz, J. R. *J. Phys. Chem. B* **2004**, *108*, 19114−19118.

(13) Chowdhury, M. H.; Ray, K.; Gray, S. K.; Pond, J.; Lakowicz, J. R. *Anal. Chem.* **2009**, *81*, 1397−1403.

(14) Taguchi, A.; Hayazawa, N.; Furusawa, K.; Ishitobi, H.; Kawata, S. *J. Raman Spectrosc.* **2009**, *40*, 1324−1330.

(15) Jha, S. K.; Ahmed, Z.; Agio, M.; Ekinci, Y.; Löffler, J. F. *J. Am. Chem. Soc.* **2012**, *134*, 1966−1969.

(16) Canalejas-Tejero, V.; Herranz, S.; Bellingham, A.; Moreno-Bondi, M. C.; Barrios, C. A. *ACS Appl. Mater. Interfaces* **2014**, *6*, 1005−1010.

(17) Nelayah, J.; Kociak, M.; Stéphan, O.; García De Abajo, J.; Tencé, M.; Henrard, L.; Taverna, D.; Pastoriza-Santos, I.; Liz-Marzán, L. M.; Colliex, C. *Nat. Phys.* **2007**, *3*, 348−353.

(18) Bosman, M.; Keast, V. J.; Watanabe, M.; Maaroof, A. I.; Cortie, M. B. *Nanotechnology* **2007**, *18*, 165505.

(19) García De Abajo, J.; Kociak, M. *Phys. Rev. Lett.* **2008**, *100*, 106804.

(20) García De Abajo, J. *Rev. Mod. Phys.* **2010**, *82*, 209−275.

(21) Kociak, M.; Stéphan, O. *Chem. Soc. Rev.* **2014**, *43*, 3865−3883.

(22) Lerondel, G.; Kostcheev, S.; Plain, J. In *Plasmonics*, Springer Series in Optical Sciences; Springer: Berlin, 2012; Vol. *167*, pp 269−316.

(23) Gloter, A.; Douiri, A.; Tencé, M.; Colliex, C. *Ultramicroscopy* **2003**, *96*, 385−400.

(24) Batson, P. E. *Ultramicroscopy* **1982**, *9*, 277−282.

(25) Mazzucco, S.; Stéphan, O.; Colliex, C.; Pastoriza-Santos, I.; Liz-Marzán, L. M.; Garcia de Abajo, J.; Kociak, M. *Eur. Phys. J.: Appl. Phys.* **2011**, *54*, 33512.

(26) Nelayah, J.; Kociak, M.; Stéphan, O.; Geuquet, N.; Henrard, L.; García De Abajo, J.; Pastoriza-Santos, I.; Liz-Marzán, L. M.; Colliex, C. *Nano Lett.* **2010**, *10*, 902−907.

(27) Gu, L.; Sigle, W.; Koch, C. T.; Ögüt, B.; van Aken, P. A.; Talebi, N.; Vogelgesang, R.; Mu, J.; Wen, X.; Mao, J. *Phys. Rev. B* **2011**, *83*, 195433.

(28) Ross, B.; Lee, L. P. *Opt. Lett.* **2009**, *34*, 896−898.

(29) Nicoletti, O.; Wubs, M.; Mortensen, N. A.; Sigle, W.; van Aken, P. A.; Midgley, P. A. *Opt. Express* **2011**, *19*, 15371.

(30) Rossouw, D.; Couillard, M.; Vickery, J.; Kumacheva, E.; Botton, G. A. *Nano Lett.* **2011**, *11*, 1499−1504.

(31) Schider, G.; Krenn, J. R.; Hohenau, A.; Ditlbacher, H.; Leitner, A.; Aussenegg, F. R.; Schaich, W.; Puscasu, I.; Monacelli, B.; Boreman, G. *Phys. Rev. B* **2003**, *68*, 155427.

(32) Hohenester, U.; Trügler, A. *Comput. Phys. Commun.* **2012**, *183*, 370−381.

(33) Hohenester, U. *Comput. Phys. Commun.* **2014**, *185*, 1177−1187.

(34) Lecarme, O.; Sun, Q.; Ueno, K.; Misawa, H. *ACS Photonics* **2014**, *1*, 538−546.

(35) García De Abajo, J.; Howie, A. *Phys. Rev. B* **2002**, *65*, 115418.

(36) Novo, C.; Funston, A. M.; Pastoriza-Santos, I.; Liz-Marzán, L. M.; Mulvaney, P. *J. Phys. Chem. C* **2008**, *112*, 3−7.

(37) Hubert, C.; Bachelot, R.; Plain, J.; Kostcheev, S.; Lerondel, G.; Juan, M. L.; Royer, P.; Zou, S.; Schatz, G. C.; Wiederrecht, G. P.; Gray, S. K. *J. Phys. Chem. C* **2008**, *112*, 4111−4116.

(38) Alber, I.; Sigle, W.; Müller, S.; Neumann, R.; Picht, O.; Rauber, M.; van Aken, P. A.; Toimil-Molares, M. E. *ACS Nano* **2011**, *5*, 9845−9853.

(39) Zoric, I.; Zäch, M.; Kasemo, B.; Langhammer, C. *ACS Nano* **2011**, *5*, 2535−2546.

(40) Sönnichsen, C.; Franzl, T.; Wilk, T.; von Plessen, G.; Feldmann, J.; Wilson, O.; Mulvaney, P. *Phys. Rev. Lett.* **2002**, *88*, 077402.

(41) Zhang, S.; Chen, L.; Huang, Y.; Xu, H. *Nanoscale* **2013**, *5*, 6985−6991.

(42) Arenal, R.; Stéphan, O.; Kociak, M.; Taverna, D.; Loiseau, A.; Colliex, C. *Phys. Rev. Lett.* **2005**, *95*, 127601.

(43) Boudarham, G.; Kociak, M. *Phys. Rev. B* **2012**, *85*, 245447.